Available online at www.sciencedirect.com

ScienceDirect

Advances in Space Research 53 (2014) 1153–1161

ADVANCES IN SPACE RESEARCH (a COSPAR publication)

www.elsevier.com/locate/asr

Energization of charged particle in a time-dependent chaotic magnetic field with an implication of the production of seed particles in solar energetic particle events

Xiaocan Li [a], Brahmananda Dasgupta [b], Gang Li [a,b,*]

[a] Department of Space Science, University of Alabama in Huntsville, AL 35899, United States
[b] CSPAR, University of Alabama in Huntsville, AL 35899, United States

Received 13 July 2013; received in revised form 8 November 2013; accepted 8 January 2014
Available online 18 January 2014

Abstract

We investigate the acceleration of charged particles in a time-dependent chaotic magnetic field in this work. In earlier works, it has been demonstrated that in an asymmetric wire-loop current systems (WLCSs), the magnetic field is of chaotic in nature. Furthermore, observations also showed that there exist time-varying current loops and current filaments in solar corona. It is therefore natural to conceive that the magnetic field on the solar surface is chaotic and time-dependent. Here, we develop a numerical model to study the acceleration process of charged particles in a time-varying chaotic magnetic field that is generated by an ensemble of 8 WLCSs. We found that the motion of energetic particles in the system is of diffusive in nature and a power law spectrum can quickly develop. The mechanism examined here may serve as an efficient pre-acceleration mechanism that generates the so-called seed particles for diffusive shock acceleration at a coronal mass ejection (CME) driven shock in large solar energetic particle (SEP) events.

Keywords: Wire-loop current systems; Chaotic fields; Seed particles; Solar energetic particle (SEP) events

1. Introduction

Particles up to 1 GeV are accelerated at the Sun through either solar flares or coronal mass ejections (CMEs). In large solar energetic particle (SEP) events, flares and CMEs often co-exist, making the identification of the acceleration site difficult (Cane et al., 2003; Li and Zank, 2005). Nevertheless, it is believed that, at least in large gradual SEP events, particles are efficiently accelerated at the CME-driven shock (Reames, 1999). Recent studies have shown that it is the suprathermal population that is preferentially accelerated in SEP events (Mason et al., 1999; Cohen et al., 2003; Desai et al., 2006). Where do these suprathermal ions come from and what is the acceleration mechanism of these suprathermal particles has been an unresolved question in space plasma physics.

Two widely accepted mechanisms of particle acceleration in space plasma are shock acceleration and stochastic acceleration. Shock acceleration is also known as "first order" Fermi acceleration, while stochastic acceleration is sometimes referred to as "second order" Fermi acceleration. A nice discussion of these two different acceleration mechanisms in the context of solar physics can be found in the review of Miller et al. (1997). The main difference between the "first order" Fermi acceleration and the "second order" Fermi acceleration is that the collisions in the former are coherent while that in the latter are random. In the context of solar flares, both mechanisms have been explored (Mann et al., 1999; Miller, 1998; Li et al., 2013). In both mechanisms, electric field does not need to be invoked explicitly, one can understand the acceleration

* Corresponding author at: Department of Space Science, University of Alabama in Huntsville, AL 35899, United States. Tel.: +1 256 961 7310; fax: +1 256 961 7730.
E-mail address: gang.li@uah.edu (G. Li).

0273-1177/$36.00 © 2014 COSPAR. Published by Elsevier Ltd. All rights reserved.
http://dx.doi.org/10.1016/j.asr.2014.01.008

process by changing reference frames and assuming the "collisions" (between particles and various plasma waves) conserve particle's energy in the instantaneous local wave frame. Alternatively, one can include electric fields explicitly, as done, for example, by Litvinenko (1996) and Matthaeus et al. (1984). In the stochastic acceleration mechanism, the acceleration is due to small scale turbulence field, so the large scale structure of the magnetic field and in particular the existence of large scale electric currents was not considered. In a test particle simulation (Giacalone and Jokipii, 1999, e.g.), the effect of the turbulent δB field is taken into account often by performing a Fourier transform of a prescribed power spectrum $I(k)$. Particle trajectories and energies are then numerically followed within this prescribed magnetic field. This prescribed magnetic field is, however, not chaotic.

Observations from various solar missions (GOES, SOHO, Yohkoh, RHESSI, Hinode, SDO, etc.) (Fletcher et al., 2011; Marsch et al., 2004; Demidov and Balthasar, 2009; Sterling et al., 2012; Sun et al., 2012) have revealed that the structure of solar magnetic fields (in particular, of the active region magnetic field), are extremely complex and variable in time. Of these complex structures, some fundamental forms, for example, current loops, current-sheets and linear elements can be identified. Radio astronomical observations of Faraday rotation in the solar corona can be interpreted as evidence for coronal currents, with values as large as 2.5×10^9 A (Spangler, 2007). Mikic et al., 1989 demonstrated that current filaments can be created in solar corona through braidings that produced by smooth, randomly phased photospheric flows. The reconnection caused by these braidings has been suggested previous by Gold and Parker to account for coronal heating (Gold, 1964; Parker, 1972). Work by Tajima et al. (1982) on current-loop coalescence in solar flares implied that the current-loop interaction process can lead to rich variety of physical mechanics like rapid magnetic energy conversion through partial or complete magnetic reconnection, prompt high-energy particle acceleration and other processes. In a series of papers, Sakai and Ohsawa (1988), Sakai and De Jager (1996) and Sakai et al. (2006) examined extensively how particles are accelerated during current loop coalescence in solar flares.

One notable feature of a system with complex electric current configurations is that the magnetic field due to these currents is chaotic (Dasgupta and Ram, 2007; Li et al., 2009; Ram and Dasgupta, 2010; Dasgupta et al., 2012). Therefore we expect the magnetic field at the solar corona is chaotic. If these currents are further time dependent, then the resulting chaotic magnetic field is also time-dependent, which will lead to a time-dependent chaotic electric field through Faraday's law. In a chaotic electric field, one expect charged particles are subject to acceleration, likely via the second-order Fermi acceleration mechanism (Li et al., 2009; Dasgupta et al., 2012).

In this work we study particle acceleration in a time-dependent chaotic electric field that results from a time dependent chaotic magnetic field using a numerical approach. Our study is performed in the context of solar corona where electric currents ubiquitously exist. However, we note that this is a very general acceleration process and may applicable to other astrophysical settings. To assess the effect of a chaotic magnetic field, clearly we need to construct a numerical model that contains a chaotic magnetic field. To achieve that, we can not rely on a prescribed turbulence power spectrum approach as adopted in Giacalone and Jokipii (1999) to construct the magnetic field. Instead we construct a time-dependent chaotic magnetic field that is due to a simple configuration of currents as described in our earlier works Dasgupta and Ram (2007), Li et al. (2009), Ram and Dasgupta (2010) and Dasgupta et al. (2012). We then examine charged particle acceleration in such a field. Our model of the magnetic field by a simple configuration of currents is not meant to be a realistic representation of the solar magnetic field. It, however, is chaotic, which is a feature largely ignored by previous studies of solar magnetic field.

In the following, we describe our model setup in Section 2. In Section 3, we discuss the numerical procedure (of tracing single particle's motion) used in this work. In Section 4, we examine the running diffusion coefficient D_{rr} and the particle energy spectrum. We discuss our results and conclude in Section 5.

2. The ensemble of wire loop current system

Dasgupta and Ram (2007), Li et al. (2009) and Ram and Dasgupta (2010) have discussed the time independent chaotic magnetic field due to simple wire-loop current system (WLCS). The system consists of a circular loop and a straight wire with an infinite length. When the wire passes through the center of the loop and is perpendicular to the plane of the loop, the system is in a symmetric configuration and the resulting magnetic field is non-chaotic. When the wire is tilted and/or shifted from the center of the loop, the system becomes asymmetric and the resulting magnetic field becomes chaotic. The advantage of the WLCS is that it allows analytic expressions for the magnetic and electric fields to be obtained.

The magnetic field of a static infinite straight wire current is, in spherical coordinates, $\boldsymbol{B} = \frac{2I}{cr\sin\theta}\hat{\boldsymbol{\phi}}$. The vector potential and magnetic field for a circular loop current, has been discussed in detail in, e.g., Jackson and Fox, 1999. In the case that the current in the wire varies sinusoidally with time, which we refer to as the "basic time-varying configuration", the time-dependent (retarded) vector potential can be obtained from the Green's function method,

$$\boldsymbol{A}(\boldsymbol{x},t) = \frac{1}{c}\int \frac{[\boldsymbol{J}(\boldsymbol{x}',t')]_{ret}}{R}\,d^3x' \tag{1}$$

where the suffix *ret* indicates retarded time $t' = t - R/c; R = |\boldsymbol{x} - \boldsymbol{x}'|$. Here, $\boldsymbol{J}(\boldsymbol{x}',t') = \hat{\boldsymbol{z}} I\cos(\omega t')$. It is

readily shown that the integration in Eq. (1) will lead to (see A for detailed derivations),

$$\boldsymbol{A}(\boldsymbol{x},t)=\hat{\boldsymbol{z}}\frac{2I}{c}\left[-\frac{\pi}{2}Y_0(\omega\rho/c)\cos(\omega t)+\frac{\pi}{2}J_0(\omega\rho/c)\sin(\omega t)\right] \tag{2}$$

where $J_n(x)$ and $Y_n(x)$ are the nth order Bessel functions of first and second kind, respectively; ω is the frequency of the current in the straight wire, and ρ is the minimum distance from $\boldsymbol{x}$ to the wire. In a local Cartesian coordinate system where the wire is along $\hat{\boldsymbol{z}}$ direction and pass through the origin, $\rho=\sqrt{x^2+y^2}$. From the vector potential, one obtains the corresponding electric and magnetic fields,

$$E_z=-\frac{\pi I\omega}{c^2}[Y_0(\omega\rho/c)\sin(\omega t)+J_0(\omega\rho/c)\cos(\omega t)] \tag{3}$$

$$B_\phi(\rho,t)=\frac{\pi I\omega}{c^2}[-Y_1(\omega\rho/c)\cos\omega t+J_1(\omega\rho/c)\sin\omega t] \tag{4}$$

To approximate the magnetic field in the solar corona that is above an AR, we consider here an ensemble of eight WLCSs. We emphasize that we make no claims that an ensemble of eight WLCSs can represent the realistic magnetic field near solar active regions. However, a system of 8 WLCSs is more complex comparing to a single WLCSs, while at the same time is still computational tractable. These make studying this system attractive.

The configuration of the ensemble of 8 WLCSs in our system is shown in Fig. 1. The left panel of Fig. 1 shows a single WLCS. The blue circle is a current loop and the red line is a current wire. The wire is off by a shift Δr from the loop center and an inclination angle θ_0 from the $\hat{z}$ direction. In the right panel, the ensemble system of 8 WLCSs is shown. There are two cubes shown in the right panel. The black dashed line outlines the inner cube. Located at each corner of the inner cube is a single WLCS. The size of the cube is 2.5 L_0, where L_0 is the radius of all loops (set to be equal). We set $L_0=6.96\times10^8$ cm $\sim 0.01R_\odot$, which is of typical size of a solar AR. The directions of all wires and the normal directions of all loops are arbitrarily chosen. The wires are shifted from the loop center by an arbitrary amount between 0.01 L_0 and 0.03 L_0. The currents in all wires are set to be 1.0 I_0 and the currents in all loops 5.0 I_0, with $I_0=4.0\times10^8$ A, a typical value found in solar AR (Spangler, 2007). The outer cubes (outlined by the green dashed lines) denotes the simulation box. Particles reach this box from inside will escape. The length of the side of the outerbox is set to be 7.5 L_0.

To see the chaotic nature of the magnetic field, we trace the field lines using the field line equations, which, in spherical coordinates, is,

$$\frac{dr}{B_r}=\frac{r d\theta}{B_\theta}=\frac{r\sin\theta d\phi}{B_\phi}=\frac{ds}{|B|}. \tag{5}$$

Fig. 2 is a 3-D plot of three field lines of the system. These field lines are close to each other when they are near the center of the cube. The x-coordinates of them are $x=1.24$ (red), 1.25 (green), and 1.26 (blue) respectively. Their y and z coordinates are the same with $y=1.25$ and $z=1.25$ (all lengths are in unit of L_0). Although these field lines are closer at their initial locations, they differ much at other places and their separations are unpredictable, as in a chaotic system.

With this ensemble of WLCSs, we perform statistical studies on particle's motion and acceleration by following the trajectories of single charged particles. We consider only proton in this work. Ions are similar. We do not consider electron in this work because the time step for electrons is $\sim$ 1840 times smaller than protons and this posts a strong constraint to our computational capability. It takes over 5 h to obtain a spectrum of proton as shown in Fig. 6 for our current simulation. We defer the consideration for electrons to a future work. Specifically, we calculate the running diffusion coefficients of protons in the configuration space to examine if their motion is of diffu-

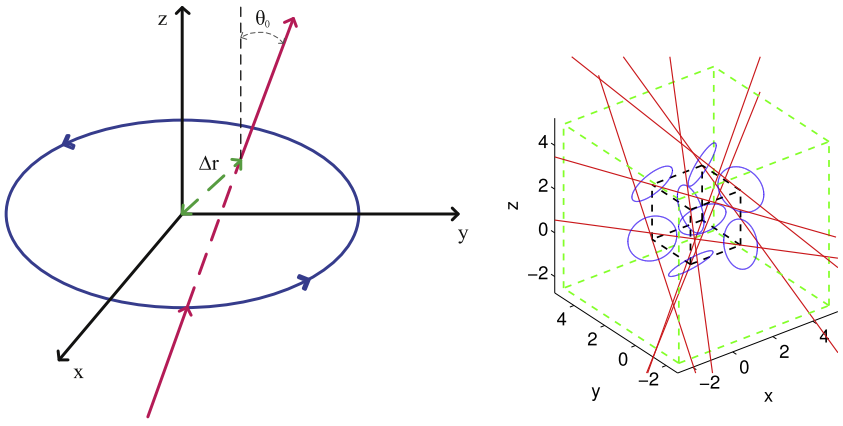

Fig. 1. Setup of the system. Left panel: a single WLCS. The blue circle is a current loop. The red straight line is a current wire. The wire is off from the loop center by a translation of Δr and an inclination of θ_0 from the $\hat{z}$ direction. Right panel: An ensemble of eight WLCSs. These WLCSs exist at the eight corners of the inner cube (black dashed line). The radii of all loops are L_0, and $L_0=6.96\times10^8$ cm. The currents in all wires are I_0 and the currents in all loops are $5.0I_0$, with $I_0=4.0\times10^8$ A. (For interpretation of the references to colour in this figure caption, the reader is referred to the web version of this article.)

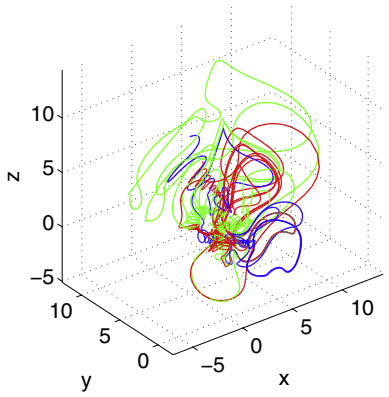

Fig. 2. 3D plots of three magnetic field lines of the current system shown in Fig. 1. The magnetic fields are traced from three close positions near/at the center of the cube. The x-coordinate of the starting points of the three field lines are $x = 1.24$ (red), 1.25 (green), and 1.26 (blue). Their y and z coordinates are the same with $y = 1.25$ and $z = 1.25$. (For interpretation of the references to colour in this figure caption, the reader is referred to the web version of this article.)

sive in nature. We also obtain particle's energy spectrum at various times.

3. Tracing a charged particle in a chaotic magnetic field

To follow particle's motion, we numerically integrate the Lorentz equation.

$$\frac{d\gamma\boldsymbol{\beta}}{dt} = \frac{Q}{A}\frac{e}{m_0 c}(\boldsymbol{E} + \boldsymbol{\beta} \times \boldsymbol{B}) \tag{6}$$

where e is the electron charge; Q is the proton number, and A is the nucleon number; m_0 is the particle mass (here we consider proton); γ is the Lorentz factor; $\boldsymbol{\beta} = \frac{\boldsymbol{v}}{c}$. Particles are followed until the end of the simulation time or until it escapes from the outer boundary (see Appendix B for more details).

We employ three different tracking methods, including the 4th order Runge–Kutta method (RK4), the Dormand–Prince method (Press et al., 2007) and the Wirz's Modified Boris method (WIRZ) (Mao and Wirz, 2011). The RK4 method is a general ordinary differential equation (ODE) integrator. The Dormand–Prince method is a Runge–kutta method with adaptive size control. It has higher order accuracy and runs faster than RK4 (Press et al., 2007). The WIRZ method is adapted from the Buneman–Boris particle tracker which is widely used in Particle-in-Cell (PIC) simulations (Birdsall and Langdon, 2005). It provides a better estimations of the magnetic field at each time step which is accomplished by using a corrected magnetic field values at the midpoint (Mao and Wirz, 2011). Comparisons between these three methods showed that the same particle trajectories are obtained in both the time-independent and time-dependent cases. This provides a consistency check to ensure, for example, that our numerical scheme does not introduce any artificial energy changes.

The size of our simulation box is of the order of $0.075\ R_\odot$. Since we consider a collisionless plasma, we place the simulation box at a height (measured from the center of the box to the photosphere) of $\sim 0.1\ R_\odot$. It can be placed above either the quiet solar surface or an active region and one can vary I_0 to approximate these two different scenarios. Above an active region, as we discuss below, this mechanism may provide the required seed population for a subsequent acceleration at a CME-driven shock.

We consider now the magnetic field strength in the simulation box. In Fig. 3 we plot the $\mathcal{F}(B)$, the integral percentage of the magnetic field with magnitude smaller than $|B|$. The left panel is for the inner box and the right panel for the outer box, as shown in Fig. 1. For $I_0 = 4 \times 10^8$ A, in 40% (10%) volume of the inner box the magnetic field is larger than 1 (2.5) Gauss. These percentages decrease to 10% and 2% for the larger box. These magnetic fields, on the order of a few to ~ 10 Gauss, are similar to that observed in the solar corona (see e.g. Liu, 2008). Note that to better approximate the coronal magnetic field, one can set the current the current in the lower 4 WLCS to be larger than those in the upper 4 WLCS. Here to illustrate our mechanism, however, we do not consider these set up details.

Fig. 4 plots the trajectory of two protons and their energy evolution in the 8-WLCS configuration. We assume that the current in the loop varies sinusoidally with time,

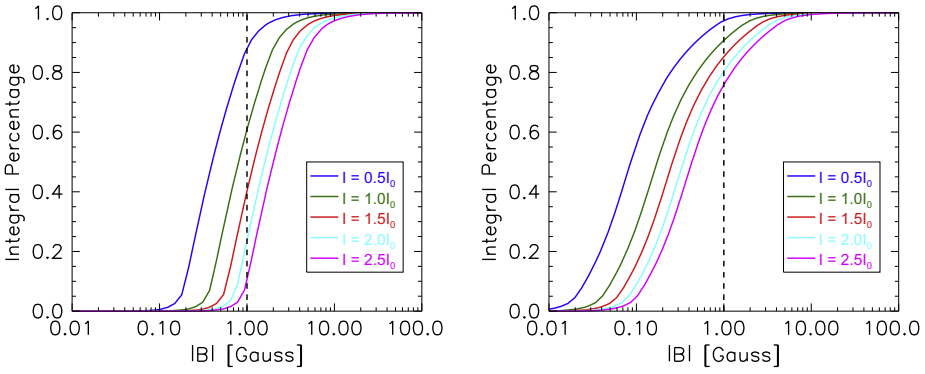

Fig. 3. $\mathcal{F}(B)$, the integral percentage of magnetic field with magnitude smaller than $|B|$. $I_0 = 4.0 \times 10^8$ A here. Left panel (right panel) is for the inner (outer) box shown in Fig. 1.

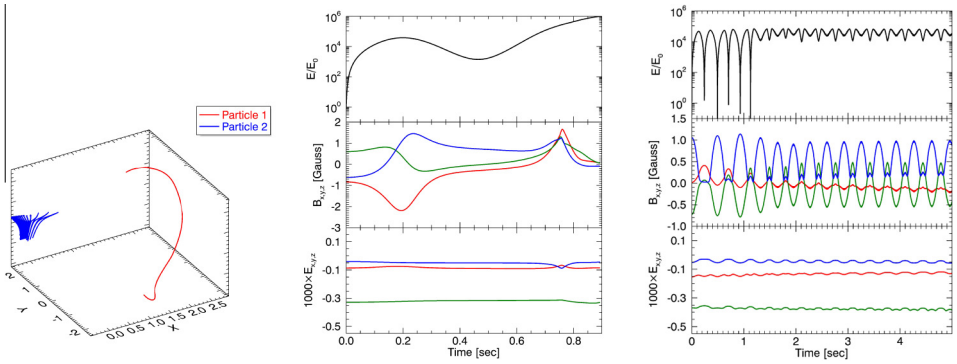

Fig. 4. Trajectory and energy evolution of two protons in a time-varying chaotic magnetic field generated by the 8-WLCS system. Left: A 3-D view of the particle trajectory. Different colors correspond to different particles. Middle: from top to bottom, for particle one, the kinetic energy E/E_0, at the **B** and **E** at the particle location (in the inertial frame). Right: the same as the middle panel, but for particle 2.

with a frequency of $\omega = 0.01$ Hz. Such a frequency corresponds to a period of 10minutes. This is comparable to the characteristic time scales found in the Sun (see e.g. Roberts, 2000). The initial energy of the particle is set to be 250 eV, corresponding to the thermal energy of a temperature $\sim 2 \times 10^6$ K. The time step Δt is chosen to be $1.0 \times 10^{-5} s$. Increasing the time step to 2.0×10^{-5} s yields the same result. The left panel shows the 3-D trajectories of these two particles: red curve is for the first particle and blue curve for the second particle. The middle panel is for the first particle. From top to bottom, it shows the kinetic energy E/E_0, and the 3 components of **B** and **E** evaluated at the particle location. The right panel is the same as the middle panel but for the second particle.

The trajectories of these two particles are very different. While the second particle stays very confined within the simulation box, the first particle moves out very quickly. The energy of the first particle increases very quickly at the beginning and then drops slightly before it increases again. In comparison, the energy of the second particle shows a clear oscillation pattern. This is because that as the second particle moves, it samples the oscillating electric field that have opposite phases. This can be also seen from the magnetic field and the electric field at the particle location.

4. Results

4.1. Particle diffusion

In many astrophysical problems, the motion of charged particles are assumed to be diffusive in nature. For example, Parker's cosmic ray transport equation implicitly assumes that cosmic ray's motion in the solar system is diffusive (Parker, 1965). In a collisionless plasma such as the solar wind, this diffusion is due to the interaction between the charged particle and the irregular turbulent magnetic field δB of the solar wind (Jokipii, 1966; Jokipii, 1971). In the case of a slab turbulence (where the k vector of the turbulent field is along the B_0 direction), this interaction leads to a diffusion coefficient $\kappa_\parallel$ whose value is decided by the power density $\delta^2 B$ of the turbulent field. The corresponding motion of the charged particle is a diffusion along the background magnetic field. Charge particles can also diffuse in the direction perpendicular to the background field B_0. Comparing to parallel diffusion, the nature of perpendicular diffusion is more perplexing. For example, at one hand, dropouts in many solar energetic particle (SEP) events (Mazur et al., 2000) tend to suggest a small transverse diffusion coefficient; on the other hand, the enhanced access of charged particles to widely disparate latitudes in the heliosphere (Maclennan et al., 2001) seems to argue an enhanced perpendicular diffusion. Recently, Li (2007), Li (2008) and Miao et al. (2011) have shown that there exist numerous current sheets in the solar wind across which the magnetic field direction change abruptly. Among other effects, the presence of these current sheets greatly enhances the perpendicular diffusion coefficient $\kappa_\perp$ of energetic particles (Qin and Li, 2008).

For a chaotic magnetic field, an ordered background field B_0 is hard to define. Furthermore there is no turbulent magnetic field δB. Therefore, we do not consider explicitly the parallel or the perpendicular diffusion. Instead, we follow the Taylor–Green–Kubo (TGK) formulation (Kubo, 1957) and calculate the running diffusion coefficient $D_{rr}(t)$ (Qin et al., 2002), which is defined as,

$$D_{rr}(t) = \frac{\left\langle (\boldsymbol{r} - \boldsymbol{r}_0)^2 \right\rangle}{2t} \tag{7}$$

where $\langle \cdots \rangle$ indicates ensemble average over all test particles; $\boldsymbol{r}$ is current position of a particle; $\boldsymbol{r}_0$ is particle's initial position; and t is the time differences between $\boldsymbol{r}$ and $\boldsymbol{r}_0$.

Fig. 5 shows the result. Two energies $E_0 = 50$ keV and $E_0 = 500$ keV are considered. A total of 6×10^3 particles are followed in each case. We use static current so that particle's energy does not change. Note, for different particles, we choose $\boldsymbol{r}_0$ randomly. This is to prevent any possible dependence of the particle trajectory on the initial location. To properly calculate D_{rr}, we follow all particles even after they escape the simulation box. Consider the case with

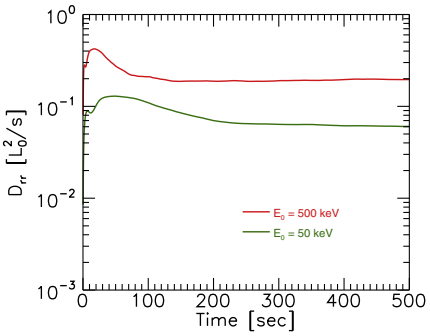

Fig. 5. Running diffusion coefficient $D_{rr}(t)$. The ensemble configuration in Fig. 1 is used. The number of the test particles is 5×10^4. Initially, particles are randomly distributed in the simulation box. See text for details.

$E_0 = 50$ keV. We see that the D_{rr}s initially increases with time. It then reaches a peak and decays and approaches a constant at late times, signaling that the particle motion reaches a diffusion phase. Note that the behavior of D_{rr} shown here is similar to that in Qin and Li (2008).

4.2. Particle energization by a chaotic magnetic field

In Fig. 6, we show the energy spectra of particles at different times in the simulation box. We start from an initial particle distribution that is Maxwellian with a temperature of 10^6 K. A total of $N = 5 \times 10^4$ particles are followed. Their initial locations are randomly distributed in the inner box as shown in the right panel of Fig. 1.

We consider two frequencies for the current in the wire: $\omega = 0.001$ Hz (shown in the left panel) and $\omega = 0.01$ Hz (shown in the right panel). The resulting spectra are similar except that the spectrum for the case of $\omega = 0.01$ Hz extending to higher energies.

Spectra for 5 different times: $t_i = \frac{i}{5} t_{max}$ for $i = 1, 2, \ldots 5$ are shown. As can be seen, the system quickly evolves. Consider the right panel where $\omega = 0.01$ Hz (corresponding to a period of 600 s), at time $t_{max} = 2$ seconds the spectrum becomes power-law like with an exponential decay. Afterward, the spectra do not change very much (not shown). For $\omega = 0.01$ Hz, The fitted power law indices are shown in the figure with the two vertical yellow line indicating the energy range for the fitting. For both cases we find a $\sim E^{-0.65}$ spectrum. The spectra do not depend on the scale of the system. Increasing the simulation box (side length) by two leads to spectra that show no noticeable differences from the current cases.

Note that these spectra are harder than E^{-1}. Such a hard spectrum is possible for particle that are accelerated via the second order Fermi mechanism. In our case, the time-dependent current induces a time-dependent electric field. As particles move, they sample electric fields with different phases, therefore their acceleration is by nature of 2nd order Fermi. Similar hard spectra have been obtained by Dauphin et al. (2007). In their work, the authors examined the acceleration and radiation of electrons and ions interacting with multiple small-scale dissipation regions. These small scale energy release regions can be, for example, magnetic reconnection sites where reconnecting current sheet (RCS) exist. At these current sheets particles are subject to be accelerated by direct electric field. In modeling an ensemble of such multiple energy release regions, Dauphin et al. (2007) used a cellular automaton model based on the concept of self-organized criticality. Dauphin et al. (2007) showed that the spectra of accelerated ions and electrons are power-law-like and for certain values of the electric field, they obtained spectra that are considerably harder than E^{-1} for both electrons and protons. Comparing to the model of Dauphin et al. (2007), in our model, the electric field is chaotic and everpresent, not only restricting to the current sheet as in Dauphin et al. (2007). However, as the number of energy release sites increases, one expects that the model examined in Dauphin et al. (2007) and ours should have many similarities.

While the spectra in Fig. 6 are very hard, they do not extend to very high energies. For the current parameters we use, appropriate to solar flare observations (Spangler, 2007), the protons are efficiently accelerated to energies to $\sim$ 1-10 MeV, which corresponds to the energy range of

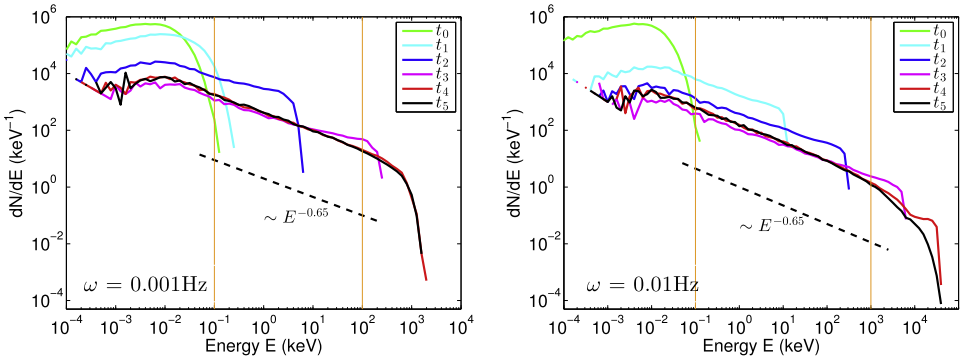

Fig. 6. Energy spectrum of protons as a function of time. Two cases are shown. The left panel has $\omega = 0.001$ Hz and the right panel has $\omega = 0.01$ Hz, where ω is the frequency of the current in the wires. A total of 5×10^4 particles are simulated for each case. The color lines indicate the energy spectra at different times. The green lines are the initial spectra. The black lines are the final spectra at $t_{max} = 2$ s ($t_{max} = 10$ s) for $\omega = 0.01$ Hz ($\omega = 0.001$ Hz). $t_0 = 0.0$ s; $t_i = \frac{i}{5} t_{max}$ for $i = 1, 2, \ldots 5$. The dashed lines are power-law fittings at t_{max} for the energy range bracketed by the two vertical yellow lines. (For interpretation of the references to colour in this figure caption, the reader is referred to the web version of this article.)

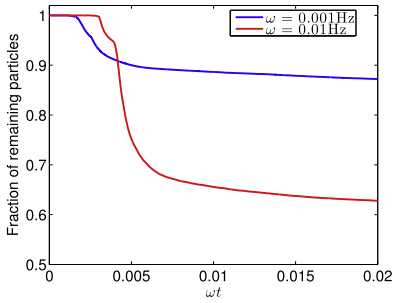

Fig. 7. Percentage of particles remained in the simulation box as a function of time. Blue line is for $\omega = 0.001$ Hz; Red line is for $\omega = 0.01$ Hz. (For interpretation of the references to colour in this figure caption, the reader is referred to the web version of this article.)

the seed population for diffusive shock acceleration process at, e.g., a CME-driven shock (see e.g. Mason et al. (1999)). Note that the injection energy at a shock depends on the shock geometry (Tylka and Lee, 2006). At a quasi-perpendicular shock, the acceleration can be fast but a high injection energy is required (Tylka and Lee, 2006). In contrast, at a quasi-parallel shock, the simulation of Li et al. (2012) showed that the injection energy can be drastically decreased. Therefore, the acceleration process we discussed here may serve as an ideal pre-acceleration site/mechanism for the seed population in large SEP events.

In calculating the spectra, we do not follow particles that reach the simulation box and assume these particles will leave the system. In the case of solar corona, if particles reach certain height, they likely encounter some open interplanetary magnetic field lines and can propagate out and be observed in situ. In comparison, those particles remain trapped in the simulation box are more likely to precipitate to the solar surface. If their energies are high, they can lead to gamma ray line emissions. In Fig. 7, we plot the percentages of trapped particles in the simulation box as a function of time. Two cases are shown with different values of $\omega = 0.001$ Hz and $\omega = 0.01$ Hz. The x-axis is ωt. It can be seen that at the beginning, the number of particles does not decrease. This is because all the particles are generated within the inner box and it takes some time for them to reach the outer box from the inner box. The number of particles then experience a quick drop, then followed by a gradual decreasing phase. For the case of $\omega = 0.001$ Hz, the amplitude of the quick drop is 10% percents. For the case of $\omega = 0.01$ Hz, the amplitude of the quick drop is 35% percents. The steady and gradual decreasing phase in both cases indicates that protons are now roughly homogeneously distributed within the simulation box and particle escaping the box can be described as a "leaky box" model.

5. Conclusion

In this work we investigate charged particle energization in a time-dependent chaotic magnetic field generated by an ensemble of simple wire-loop current system. Our work is motivated by the observation that time dependent currents are ever-present at solar surface. The presence of these currents naturally lead to a chaotic magnetic field and electric field. With the presence of electric field, charged particles are then accelerated.

The acceleration process we discuss here can occur anywhere in the solar corona. In particular, they can occur above an active region where a flare occurs. If a CME accompanies the flare, then the CME and the shock it drives can plow through these energetic particle. This makes our proposed scenario/mechanism very interesting in that it may provide the pre-acceleration mechanism for generating the seed particles for a possible subsequent diffusive shock acceleration at a Coronal-Mass-Ejection driven shock. By way of example, we assume that the electric current varies sinusoidally. The process by nature is of second order Fermi. The acceleration occurs very quick. For parameters applicable to solar corona, the energetic particle spectrum quickly (in seconds to 10's seconds) evolves to becoming power-law-like with an energy cutoff ~ 1 (~ 10) MeV for I_0 equals to 4×10^7 (4×10^8) A. The energy scales with the electric current. If a correlation exists between the pre-event current and the flare size, then our mechanism would predict that there will be more energetic seed particles in large flares.

Finally, we emphasize that our system is by no means to represent the realistic solar magnetic fields. Instead, it provides a simple and tractable system from which we can learn some fundamental behaviors of the particles in a time-dependent chaotic magnetic field, which, we believe will shed lights on our understanding of particle acceleration in solar corona. We note that some of our results, in particular, the spectra we obtained, are similar to that obtained by Dauphin et al. (2007) which is based on a different model.

Acknowledgments

This work is partially supported by NSF Grants ATM-0847719, AGS0962658; and NASA Grants NNX13AM30H and BD also acknowledges supports from NSF Grant AGS-1062050. GL and BD are also supported by two Individual Investigator Distinguished Research (IIDR) awards of the University of Alabama in Huntsville. We thank both referees for illuminating suggestions and comments.

Appendix A. Electric and magnetic fields for a Straight Wire with a time-varying current

The magnetic vector potential $\boldsymbol{A}(\boldsymbol{x}, t)$ for a time-varying current density $\boldsymbol{J}(\boldsymbol{x}, t)$ can be shown to satisfy the following equation,

$$\nabla^2 \boldsymbol{A} - \frac{1}{c^2}\frac{\partial^2 \boldsymbol{A}}{\partial t^2} = -\frac{4\pi}{c}\boldsymbol{J} \tag{A.1}$$

It can be solved in terms of the Green's function $G(\boldsymbol{x},t;\boldsymbol{x}',t')$ (Jackson and Fox, 1999), and the solution for the vector potential $\boldsymbol{A}(\boldsymbol{x},t)$ is

$$\boldsymbol{A}(\boldsymbol{x},t)=\frac{1}{c}\int\frac{[\boldsymbol{J}(\boldsymbol{x}',t')]_{ret}}{R}d^3x \tag{A.2}$$

where the suffix *ret* indicates the retarded time $t'=t-R/c$; $R=|\boldsymbol{x}-\boldsymbol{x}'|$. We assume that the current of the wire has a simple sinusoidal time variation at all points, i.e., $\boldsymbol{J}(\boldsymbol{x}',t')=\hat{\boldsymbol{z}}I\cos(\omega t')$, so that

$$[\boldsymbol{J}(\boldsymbol{x}',t')]_{ret}=\hat{\boldsymbol{z}}I\cos[\omega(t-R/c)] \tag{A.3}$$

The resulting vector potential can be expressed as

$$\boldsymbol{A}(\boldsymbol{x},t)=\lim_{L\to\infty}\hat{\boldsymbol{z}}\frac{I}{c}\int_{-L}^{L}\frac{\cos[\omega(t-R/c)]}{R}dz';\quad R=\sqrt{\rho^2+z'^2} \tag{A.4}$$

$$=\hat{\boldsymbol{z}}\frac{2I}{c}\left[\cos(\omega t)\lim_{L\to\infty}\int_{\rho}^{\sqrt{\rho^2+L^2}}\frac{\cos[\omega R/c]}{\sqrt{R^2-\rho^2}}dR+\sin(\omega t)\lim_{L\to\infty}\int_{\rho}^{\sqrt{\rho^2+L^2}}\frac{\sin[\omega R/c]}{\sqrt{R^2-\rho^2}}dR\right] \tag{A.5}$$

$$=\hat{\boldsymbol{z}}\frac{2I}{c}\left[-\frac{\pi}{2}Y_0(\omega\rho/c)\cos(\omega t)+\frac{\pi}{2}J_0(\omega\rho/c)\sin(\omega t)\right] \tag{A.6}$$

where we have used the integral representations of Bessel functions of first and second kind (Abramowitz and Stegun, 1964).

The resulting electric field $\boldsymbol{E}$ can be obtained as,

$$\boldsymbol{E}=-\nabla\phi-\frac{1}{c}\frac{\partial\boldsymbol{A}}{\partial t}=-\frac{1}{c}\frac{\partial\boldsymbol{A}}{\partial t} \tag{A.7}$$

$$=-\hat{\boldsymbol{z}}\frac{\pi I\omega}{c^2}[Y_0(\omega\rho/c)\sin(\omega t)+J_0(\omega\rho/c)\cos(\omega t)] \tag{A.8}$$

where we have let $\phi=0$ by a suitable choice of gauge (in absence of any electric charge. It is easy to see that for $\omega\to 0,\boldsymbol{E}\to 0$. The time dependent magnetic field $\boldsymbol{B}(\rho,t)$ can be evaluated from $\boldsymbol{B}(\rho,t)=\nabla\times\boldsymbol{A}(\rho,t)$. In cylindrical coordinates, the only non-vanishing component of $\boldsymbol{B}(\rho,t)$ is $B_\phi(\rho,t)$, which is given by

$$\boldsymbol{B}_\phi(\rho,t)=-\frac{\partial A_z(\rho,t)}{\partial\rho} \tag{A.9}$$

$$=\frac{\pi I}{c}\left[\frac{\partial Y_0(\omega\rho/c)}{\partial\rho}\cos\omega t-\frac{\partial J_0(\omega\rho/c)}{\partial\rho}\sin\omega t\right] \tag{A.10}$$

$$=\frac{\pi I\omega}{c^2}[-Y_1(\omega\rho/c)\cos\omega t+J_1(\omega\rho/c)\sin\omega t] \tag{A.11}$$

Define a dimensionless variable $x=\frac{\omega\rho}{c}$ and notice that the magnetic field of a straight wire $B=2I/c\rho$ in the cgs unit system is

$$\frac{B}{\text{Gauss}}=\frac{1}{5}\frac{I/\text{Ampere}}{\rho/\text{cm}}, \tag{A.12}$$

we obtain,

$$\frac{\boldsymbol{E}(\rho,t)}{\text{Gauss}}=-\hat{\boldsymbol{z}}\frac{1}{5}\frac{I/\text{Amp}}{\rho/\text{cm}}\frac{\pi x}{2}[Y_0(x)\sin(\omega t)+J_0(x)\cos(\omega t)] \tag{A.13}$$

$$\frac{\boldsymbol{B}(\rho,t)}{\text{Gauss}}=\hat{\phi}\frac{1}{5}\frac{I/\text{Amp}}{\rho/\text{cm}}\frac{\pi x}{2}[-Y_1(x)\cos\omega t+J_1(x)\sin\omega t] \tag{A.14}$$

Appendix B. Numerical integration of the Lorentz equation

Here we consider the Lorentz equation,

$$\frac{d\gamma\boldsymbol{\beta}}{dt}=\frac{Q}{A}\frac{e}{m_0c}(\boldsymbol{E}+\boldsymbol{\beta}\times\boldsymbol{B}) \tag{B.1}$$

where e is the charge of electron; Q is the charge state; A is the atom number; m_0 is the particle mass (here we consider proton); γ is the Lorentz factor; $\boldsymbol{\beta}=\frac{\boldsymbol{v}}{c}$. Writing explicitly,

$$\frac{d\gamma\boldsymbol{\beta}}{dt}=9.6\times10^3\frac{Q}{A}(\boldsymbol{E}+\boldsymbol{\beta}\times\boldsymbol{B}) \tag{B.2}$$

using the expressions of $\boldsymbol{E}$ and $\boldsymbol{B}$ in Appendix A, we have

$$\frac{\omega}{\text{Hz}}\frac{d\gamma\boldsymbol{\beta}}{d\omega t}=9.6\times10^2\frac{Q}{A}\frac{I/\text{Amp}}{\rho/\text{cm}}\pi x([Y_0(x)\sin(\omega t)+J_0(x)\cos(\omega t)]+\boldsymbol{\beta}\times\hat{\phi}[-Y_1(x)\cos\omega t+J_1(x)\sin\omega t]\Big) \tag{B.3}$$

For the problem we are considering, we can define two dimensionless quantities $\tilde{\rho}=\rho/L_0$ and $\widetilde{I}=I/I_0$ with $L_0=6.96\times10^8$ cm ($\sim 0.01\ \mathrm{R}_\odot$) and $I_0=4\times10^7$ A. This allow us to finally obtain,

$$\frac{d\gamma\boldsymbol{\beta}}{d\omega t}=55.1\frac{Q}{A}\frac{\widetilde{I}}{\tilde{\rho}}\pi x\left(\frac{\text{Hz}}{\omega}\right)([Y_0(x)\sin(\omega t)+J_0(x)\cos(\omega t)]+\boldsymbol{\beta}\times\hat{\phi}[-Y_1(x)\cos\omega t+J_1(x)\sin\omega t]\Big) \tag{B.4}$$

where

$$x=2.32\times10^{-2}\times\tilde{\rho}\frac{\omega}{\text{Hz}} \tag{B.5}$$

References

Abramowitz, M., Stegun, I.A., 1964. Handbook of Mathematical Functions: With Formulars, Graphs, and Mathematical Tables. Dover Publications.

Birdsall, C.K., Langdon, A.B., 2005. Plasma Physics via Computer Simulation. CRC Press.

Cane, H., von Rosenvinge, T., Cohen, C., Mewaldt, R., 2003. Two components in major solar particle events. Geophys. Res. Lett. 30 (12), 8017.

Cohen, C., Mewaldt, R., Cummings, A., Leske, R., Stone, E., Von Rosenvinge, T., Wiedenbeck, M., 2003. Variability of spectra in large solar energeticparticle events. Adv. Space Res. 32 (12), 2649–2654.

Dasgupta, B., Li, G., Li, X., Ram, A., 2012. Particle transport and acceleration in a chaotic magnetic field: implications for seed population to solar flare and CME. In: AIP Conference Proceedings, vol. 1500, p. 56.

Dasgupta, B., Ram, A., 2007. Chaotic magnetic fields due to asymmetric current configurations-application to cross-field diffusion of particles in cosmic rays. Bull. Am. Phys. Soc. 52.

Dauphin, C., Vilmer, N., Anastasiadis, A., 2007. Particle acceleration and radiation in flaring complex solar active regions modeled by cellular automata. Astron. Astrophys. 468 (1), 273–288.

Demidov, M.L., Balthasar, H., 2009. Spectro-polarimetric observations of solar magnetic fields and the soho/mdi calibration issue. Solar Physics 260 (2), 261–270.

Desai, M., Mason, G., Gold, R., Krimigis, S., Cohen, C., Mewaldt, R., Mazur, J., Dwyer, J., 2006. Heavy-ion elemental abundances in large solar energetic particle events and their implications for the seed population. Astrophys. J. 649 (1), 470.

Fletcher, L., Dennis, B.R., Hudson, H.S., Krucker, S., Phillips, K., Veronig, A., Battaglia, M., Bone, L., Caspi, A., Chen, Q., et al., 2011.

An observational overview of solar flares. Space Sci. Rev. 159 (1–4), 19–106.
Giacalone, J., Jokipii, J.R., 1999. The transport of cosmic rays across a turbulent magnetic field. Astrophys. J. 520 (1), 204.
Gold, T., 1964. Magnetic energy shedding in the solar atmosphere. NASA Special Publication 50, 389.
Jackson, J.D., Fox, R.F., 1999. Classical electrodynamics. Am. J. Phys. 67, 841.
Jokipii, J., 1966. Cosmic-ray propagation. i. Charged particles in a random magnetic field. Astrophys. J. 146, 480.
Jokipii, J., 1971. Propagation of cosmic rays in the solar wind. Rev. Geophys. 9 (1), 27–87.
Kubo, R., 1957. Statistical-mechanical theory of irreversible processes. i. General theory and simple applications to magnetic and conduction problems. J. Phys. Soc. Japan 12 (6), 570–586.
Li, G., Dasgupta, B., Webb, G., Ram, A., 2009. Particle motion and energization in a chaotic magnetic field. In: AIP Conference Proceedings, vol. 1183. p. 201.
Li, G., Shalchi, A., Ao, X., Zank, G., Verkhoglyadova, O.P., 2012. Particle acceleration and transport at an oblique cme-driven shock. Adv. Space Res. 49 (6), 1067–1075.
Li, G., Kong, X., Zank, G., Chen, Y., 2013. On the spectral hardening at 300 keV in solar flares. Astrophys. J. 769 (1), 22.
Li, G., Zank, G.P., 2005. Mixed particle acceleration at cme-driven shocks and flares. Geophys. Res. Lett. 32 (2), L02101.
Li, G., 2007. Flux tubes in the fast and slow solar wind. In: AIP Conference Proceedings, vol. 932, p. 26.
Li, G., 2008. Identifying current-sheet-like structures in the solar wind. Astrophys. J. Lett. 672 (1), L65.
Liu, Y., 2008. Magnetic field overlying solar eruption regions and kink and torus instabilities. Astrophys. J. Lett. 679 (2), L151.
Litvinenko, Y., 1996. Particle acceleration in reconnecting current sheets with a nonzero magnetic field. Astrophys. J. 462, 997.
Maclennan, C., Lanzerotti, L., Hawkins, S., 2001. Populating the inner heliosphere (< 5 AU) with heavy ions. In: International Cosmic Ray Conference, vol. 8. p. 3265.
Mann, G., Jansen, F., MacDowall, R., Kaiser, M., Stone, R., 1999. A heliospheric density model and type iii radio bursts. Astron. Astrophys. 348, 614–620.
Mao, H., Wirz, R., 2011. Comparison of charged particle tracking methods for non-uniform magnetic fields. In: 42nd AIAA Plasmadynamics and Lasers Conference, 2011.
Marsch, E., Wiegelmann, T., Xia, L., 2004. Coronal plasma flows and magnetic fields in solar active regions. Astron. Astrophys. 428 (2), 629–645.
Mason, G., Mazur, J., Dwyer, J., 1999. 3he enhancements in large solar energetic particle events. Astrophys. J. Lett. 525 (2), L133.
Matthaeus, W., Ambrosiano, J., Goldstein, M., 1984. Particle acceleration by turbulent magnetohydrodynamic reconnection. Phys. Rev. Lett. 53 (15), 1449–1452.
Mazur, J., Mason, G., Dwyer, J., Giacalone, J., Jokipii, J., Stone, E., 2000. Interplanetary magnetic field line mixing deduced from impulsive solar flare particles. Astrophys. J. Lett. 532 (1), L79.
Miao, B., Peng, B., Li, G., 2011. Current sheets from ulysses observation. In: Annales Geophysicae, vol. 29, pp. 237–249 (Copernicus GmbH).
Mikic, Z., Schnack, D.D., Van Hoven, G., 1989. Creation of current filaments in the solar corona. Astrophys. J. 338, 1148–1157.
Miller, J.A., 1998. Particle acceleration in impulsive solar flares. Space Sci. Rev. 86 (1), 79–105.
Miller, J.A., Cargill, P.J., Emslie, A.G., Holman, G.D., Dennis, B.R., LaRosa, T.N., Winglee, R.M., Benka, S.G., Tsuneta, S., 1997. Critical issues for understanding particle acceleration in impulsive solar flares. J. Geophys. Res. 102 (A7), 14631–14659.
Parker, E., 1965. The passage of energetic charged particles through interplanetary space. Planet. Space Sci. 13 (1), 9–49.
Parker, E., 1972. Topological dissipation and the small-scale fields in turbulent gases. Astrophys. J. 174, 499.
Press, W., Teukolsky, S., Vetterling, W., Flannery, B., 2007. Numerical recipes. The Art of Scientific Computing,, Cambridge University Press.
Qin, G., Matthaeus, W., Bieber, J., 2002. Subdiffusive transport of charged particles perpendicular to the large scale magnetic field. Geophys. Res. Lett. 29 (4), 7.
Qin, G., Li, G., 2008. Effect of flux tubes in the solar wind on the diffusion of energetic particles. Astrophys. J. Lett. 682 (2), L129.
Ram, A., Dasgupta, B., 2010. Dynamics of charged particles in spatially chaotic magnetic fields. Phys. Plasmas 17, 122104.
Reames, D.V., 1999. Particle acceleration at the sun and in the heliosphere. Space Sci. Rev. 90, 413–491.
Roberts, B., 2000. Waves and oscillations in the corona – (invited review). Solar Physics 193 (1–2), 139–152.
Sakai, J.-I., Tsuchimoto, K., Sokolov, I., 2006. Simulation of collision of two current loops in the upper chromosphere using the two-fluid model. Astrophys. J. 642 (2), 1236.
Sakai, J.-I., De Jager, C., 1996. Solar Flares and Collisions between Current-Carrying Loops. Springer.
Sakai, J.-I., Ohsawa, Y., 1988. Particle acceleration by magnetic reconnection and shocks during current loop coalescence in solar flares. Space Sci. Rev. 46 (1–2), 113–198.
Spangler, S.R., 2007. A technique for measuring electrical currents in the solar corona. Astrophys. J. 670 (1), 841.
Sterling, A.C., Moore, R.L., Hara, H., 2012. Observations from sdo, hinode, and stereo of a twisting and writhing start to a solar-filament-eruption cascade. Astrophys. J. 761, 69.
Sun, X., Hoeksema, J.T., Liu, Y., Wiegelmann, T., Hayashi, K., Chen, Q., Thalmann, J., 2012. Evolution of magnetic field and energy in a major eruptive active region based on sdo/hmi observation. Astrophys. J. 748, 77.
Tajima, T., Brunel, F., Sakai, J., 1982. Loop coalescence in flares and coronal X-ray brightening. Astrophys. J. 258, L45–L48.
Tylka, Allan J., Lee, Martin A., 2006. A model for spectral and compositional variability at high energies in large, gradual solar particle events. Astrophys. J. 646 (2), 1319.